Differentiation Power Control of Modules in Second-Life Battery Energy Storage System Based on Cascaded H-Bridge Converter

Chang Liu, Ning Gao, Xu Cai, and Rui Li, *Member, IEEE*

***Abstract*—There is a possibility that second-life power batteries, which can store and deliver substantial energy, could satisfy the requirements of stationary energy storage applications. In this article, split second-life battery modules with good performance have been directly introduced to the dc sides of the H-bridges in cascaded H-bridge converter (CHBC) without complex manual dismantling, screening, and recombination of the battery cells. However, the severe discrepancies of the second-life battery modules' parameters can lead to overcharge, overdischarge, and underutilization of some battery modules' effective capacity simultaneously. To suitably integrate and control these widely different battery modules, a differentiation power control strategy based on the online battery parameter estimation method is proposed. Real-time online power allocation of the independent power modules according to the parameters of the battery modules is conducted by the strategy, which ensures that the charging/discharging trajectories of the second-life battery modules during a charging/discharging cycle will all arrive at their maximum/minimum values at the same time, whether the battery modules are in the same phase or different phases. The control range and capability of the strategy are also analyzed quantitatively. Finally, modeling, analysis, and experimental validation are performed on a downscaled prototype in the laboratory.**

***Index Terms*—Battery energy storage system (BESS), cascaded H-bridge converter (CHBC), differentiation power control strategy, online parameter estimation, quantitative analysis, second-life battery.**

I. Introduction

HIGH penetration of renewables on the grid and construction of the distributed microgrids, ancillary services, and so on are stimulating the growth of demand for energy storage system (ESS) [1]–[5]. Among all the ESS technologies, battery energy storage system (BESS) has been giving priority to the development because of its high power density, quick response time, small volume, and no special requirement for installation site [6]–[8]. The high cost of batteries represents a prominent barrier for widespread use of BESS in the utility grid [9]. Recently, with the promotion and application of electric vehicles (EVs) around the world, large amounts of second-life batteries will pour into the market in the near future. Usually, the EV batteries are considered depleted when they cannot provide 80% of the nominal capacity, which is needed for the vehicle range. But the depleted batteries are competent to the stationary energy storage system at reduced cost, which can not only extend the whole-life cycle of the battery, but also relieve the pressure of waste batteries' recycling and disposal [10]–[13].

Papers [14]–[17] analyzed the feasibility of second-life battery energy storage system (SLBESS) from the angle of economy, technology, and environmental impact, which has laid the groundwork for the relevant future studies. However, only a very limited number of papers have given a detailed analysis of the design from the viewpoint of the system's realization [11], [18]–[21]. Power electronics converter plays a key role in SLBESS, which can be categorized into two main types based on the interface converter. First, all the retired battery cells are assembled in one module after screening and recombination, and it is integrated with load or into the grid through a traditional two-level converter [11], [18], [19]. In [18], Tong *et al*. examined the feasibility of integrating a second-life battery module with an off-grid photovoltaic (PV) vehicle charging system. The second-life battery module is charged by a PV array with a maximum power point tracking controller, and then the battery system charges a vehicle via a two-level inverter. The second-life battery module has 135 LiFePO4 based battery cells, which have been connected in series and parallel to achieve an accessible storage capacity of 13.9 kWh. Experimental results show that the SLBESS with a simple control structure achieved the desirable function successfully. Second, the second-life battery modules are integrated into the grid through multilevel or multiport converter [20], [21]. In order to make full use of second-life batteries on the grid system, a modular boost-multilevel buck converter topology along with its module-based distributed control architecture were introduced in [20]. Second-life batteries with widely different parameters, such as module voltage, capacity, and initial state-of-charge (SOC), can be integrated to an inverter dc link flexibly under this topology and its control method. However, the proposed converter is a three-stage single phase inverter with cascaded dc links and also is inapplicable in appliances what require high power quality and large-scale

Manuscript received March 9, 2019; revised July 9, 2019; accepted November 15, 2019. Date of publication November 19, 2019; date of current version February 20, 2020. This work was supported by the National Natural Science Foundation of China under Grant 51777124. Recommended for publication by Associate Editor M. Ferdowsi. *(Corresponding author: Xu Cai.)*

C. Liu, X. Cai, and R. Li are with Wind Power Research Center, School of Electronic Information and Electrical Engineering, Shanghai Jiao Tong University, Shanghai 200240, China (e-mail: liuchangzm@sjtu.edu.cn; xucai@sjtu.edu.cn; liruiqd@sjtu.edu.cn).

N. Gao is with the Department of Electrical Engineering, Shanghai Maritime University, Shanghai 201306, China (e-mail: ngao@shmtu.edu.cn).

Color versions of one or more of the figures in this article are available online at http://ieeexplore.ieee.org.

Digital Object Identifier 10.1109/TPEL.2019.2954577

capacity. And also, capacity expansion of the SLBESS in [20] is limited and difficult. Furthermore, a three-stage converter is accompanied by low efficiency, low reliability, and complicated control strategy. In [21], three second-life battery modules were recombined by screened battery cells or modules with relatively good performance, then they were integrated to the dc bus of a three-phase grid-connected inverter through three independent dc/dc converters. Meanwhile, an energy management control strategy is proposed to distribute and control the power demand among three second-life battery modules under different load conditions and disturbances, which has been developed to integrate flexibly different levels (i.e., size, capacity, and chemistry type) of the second-life battery modules into the grid through a multiport converter. We found that all the SLBESSs mentioned above are more or less confined to small capacity, low efficiency, low reliability, and low scalability to large-scale capacity, which all aroused from the adopted converters.

Compared with the new ones, second-life batteries suffer from lower reliability because of degraded performance and failure, which will have impact on overall system reliability. Both the reliability of different single phase battery-to-grid converter interfacing schemes and second-life battery modules were calculated and compared in [22], where a CHBC with an integrated dc–dc converter scheme for robust and reliable SLBESS is recommended without taking the efficiency and volume of the system into consideration. CHBC can integrate the split low-voltage small-capacity battery module into the high-voltage grid (10–35 kV) without bulky line transformer. Thus, a higher efficiency of the whole system can be obtained and the problem of circulating current among battery cells can be solved. Also, the modular structure of CHBC improves the redundancy and reliability of CHBC-BESS. The advantages mentioned above make CHBC the most likely approach for massive BESS [23], [24].

In this article, split second-life battery modules with effective functional components have been introduced to the dc sides of the H-bridges in CHBC directly without complex screening and recombination of the battery cells. When applicated in EVs, the differences in series–parallel mode, placement, working condition, and degradation trajectory lead to widely different battery parameters, such as effective capacity, internal impedance, and so on. So, the conventional interphase or interbridge SOC balancing strategies and the control strategy for the CHBC-BESS based on the new batteries, as reported in [25], where the SOC is defined by the rated capacity, are inapplicable in second-life BESS based on cascaded H-bridge converter (CHBC-SLBESS). To make full utilization of these widely different battery modules and avoid overcharge and overdischarge of them, we redefine the SOC of the second-life battery according to the effective capacity obtained by the proposed online battery parameter estimation method, then a real-time online power allocation of the independent power modules according to the parameters of the battery modules is conducted. On the basis of these, a differentiation power control strategy of CHBC-SLBESS based on the decoupled current control of CHBC is proposed, which includes both the interphase differentiation power control and interbridge differentiation power control. The interbridge differentiation power control is implemented by introducing closed module power control loops. The interphase differentiation power control is implemented by injecting the zero-sequence voltage related to the battery parameters into the output voltage of CHBC. Meanwhile, the control ranges and interplay of the proposed interphase and interbridge differentiation power control strategy are analyzed in detail. The analysis shows that the proposed interbridge differentiation power control strategy can greatly reduce the control range of the interphase differentiation power control strategy. To address this issue, a double 1/6 third harmonic voltage injection (DTHVI) method based on the fundamental frequency zero-sequence voltage injection (FFZSVI) method was proposed to extend the control ranges of the interphase and interbridge differentiation power control strategy at the same time to the fullest possible extent. Moreover, quantitative analysis of the control range is conducted. Under the proposed differentiation power control strategy, these widely different battery modules can be fully utilized and overcharge and overdischarge of them can also be avoided. In [24], an active-power control strategy of individual power modules in CHBC-BESS was proposed, which also enables the multiple battery modules operate at different power levels. However, the power sharing strategy of the power modules is ignored in [24], so it is unclear how to allocate the power that is assumed by each power module. By comparison, our method has a clear description of the power sharing strategy and can allocate the power assumed by each power module according to their parameters. Additionally, the strategy of [24] did not take the parameters of the batteries into consideration, which makes the strategy invalid when the battery parameters change. Finally, the control range of the strategy proposed in [24] is much narrower than our method. Though our method adds more complexity to the system compared with methods proposed in [24] and [25] and its requirements for control system are high, it could reduce the cost of the whole system because second-life battery modules can be introduced to the dc sides of the H-bridges directly without screening and recombination of the battery cells under our proposed method. The rest of this article is organized as follows. Section II is devoted to the system configuration and modeling of CHBC-SLBESS. Online battery parameter estimation, distributed power sharing strategy, and differentiation power control strategy are given in Sections III–V, respectively. Experimental results from a downscaled laboratory prototype are provided in Section VI to validate the effectiveness and feasibility of the presented strategy. Finally, Section VII concludes this paper.

II. System Configuration and Modeling of CHBC-SLBESS

Fig. 1 shows the layout of a star-connected, three-phase, $2n + 1$ level CHBC-SLBESS, which consists of $3n$ power modules, each composed of H-bridge converter and its driving circuits, dc bus capacitance, dc fuse, precharge device on the dc side, and second-life battery module. When the fault of either a power device or a battery module is detected, or the fuse in series with the battery unit blows, the corresponding power module is

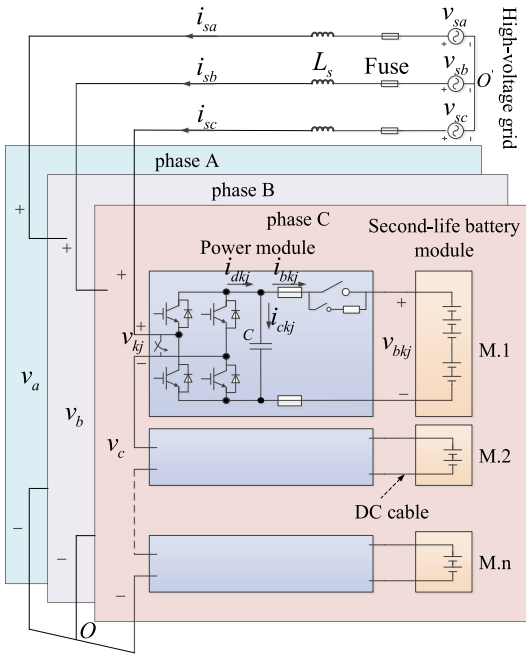

Fig. 1. System configuration of CHBC-SLBESS.

bypassed immediately by short-circuiting its ac terminal by a bidirectional switch or a bypass contactor [26]. Then, the whole system can keep running. The modular structure of CHBC allows easy extension to reach higher voltage and power levels, thus making it feasible to connect to a high-voltage grid without bulky and heavy line-frequency transformers. In Fig. 1, v_{sa}, v_{sb}, v_{sc} and i_{sa}, i_{sb}, i_{sc} represent grid voltages and currents, respectively. v_a, v_b, v_c represent the output voltages of CHBC. v_{kj}, $v_{bkj}, i_{dkj}, i_{ckj}, i_{bkj}$ represent the ac side output voltage, battery module voltage, dc side current, dc bus capacitance current, and battery module current of the *j*th power module of phase *k,* respectively ($k = a, b, c$; $j = 1, 2 \ldots, n$).

The ac sides of the H-bridge converters are connected in series, so the output voltage of CHBC is easily determined from the following equation:

$$v_k = \sum_{j=1}^{n} v_{kj} = \sum_{j=1}^{n} d_{kj} v_{bkj}, (k = a, b, c) \tag{1}$$

where d_{kj} is the switching function of the *j*th power module of phase *k*. The system's dynamic behavior can be described by (2) and (3), where $v_{oo'}$ represents the zero-sequence voltage of the system and *R* is the parasitic resistance of the filter inductance L_s

$$\begin{cases} v_{sk} - v_k - \left(L_s \frac{di_{sk}}{dt} + R i_{sk}\right) = v_{oo'} \\ v_{oo'} = \frac{1}{3}(v_{sa} + v_{sb} + v_{sc} - v_a - v_b - v_c) \end{cases} \tag{2}$$

$$\begin{cases} i_{dkj} = i_{ckj} + i_{bkj} = C \frac{dv_{bkj}}{dt} + i_{bkj} \\ i_{dkj} = d_{kj} \cdot i_{sk}. \end{cases} \tag{3}$$

As the control input of the system, the switching function d_{kj} can have the discrete values ± 1 or 0, when the output voltage of the H-bridge is $\pm v_{bkj}$ or 0, respectively. To linearize the model of the converter, the discrete switching function d_{kj} can be replaced by the continuous sinusoidal switching function s_{kj}, which is bounded in the interval $[-1, 1]$.

TABLE I
PARAMETERS OF A NEW BATTERY MODULE

Items	Parameters
Nominal voltage (V)	23
Nominal capacity (Ah)	10
Array mode	10S1P
Operating voltage range (V)	18−27.5
Rated operational current (A)	40
Maximum allowable continuous working current (A)	60
Operating temperature range (°C)	–20−+60

III. ONLINE PARAMETER ESTIMATION OF SECOND-LIFE BATTERY MODULE

Online battery parameter estimation is necessary for making full utilization of the second-life battery module's capacity. Corresponding adjustment of the proposed differentiation power control strategy should be made according to the parameter variations of the battery. The estimated parameters include internal impedance, open-circuit voltage (OCV), effective capacity, and SOC. Taking a second-life lithium titanate battery module, which was applied in the laboratory prototype and manufactured by Microvast Power Systems Co., Ltd., as an example, this section presents the process of online battery parameter estimation in detail. Table I shows the parameters of a new battery module. When first applied in EVs, the battery module functions as the basic unit, which can form the power train of the vehicle after suitable series–parallel connection.

The proposed online parameter estimation in this section performs the following steps.

Step 1: Estimate the internal impedance (*Z*) of the battery module. Fig. 3 shows the two kinds of the commonly used equivalent-circuit models of the battery, i.e., the RC model and linear model. The RC model, which includes one or several *RC* networks, the internal resistance (R_s) as well as the voltage source, which provides the predicted OCV [27], [28], [31]. The RC parallel network modeling the activation polarization or charge-transfer overvoltage and concentration polarization at anode and cathode [27] is added to implement the time constant during transient. The number of RC branches depends on the desired accuracy and bandwidth of the model [28]. One to three RC branches are typically used. We have to emphasize the fact that the RC branch model is actually an "analogue" of an electrical system rather than a model of specific electrical components (such as series internal resistance R_s) [33]. The RC model is suitable for describing the dynamic performance of the battery. The linear model is simple and suitable for describing the steady-state performance of the battery [29]. The internal resistance (R_s) of the RC model has the same value for the linear model. Then,

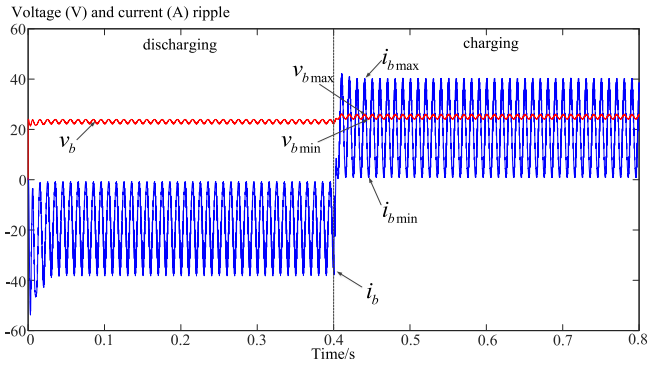

Fig. 2. Waveforms of the current and voltage of the battery module.

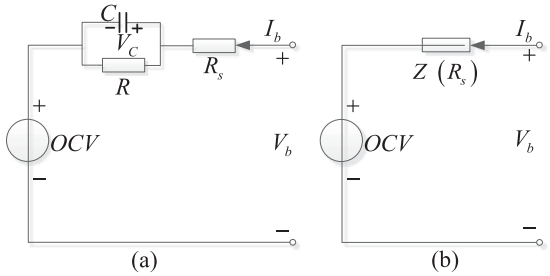

Fig. 3. Battery module's equivalent circuit. (a) RC model. (b) Linear model.

we can easily draw the conclusion that the RC model and the linear model have the same performance during the steady state of the battery [29]. This paper adopts a ripple based online internal impedance estimation method, as shown in [30]. Each cascaded single phase H-bridge converter results in the 100 Hz rippled current of the battery. At the same time, the battery voltage ripples with the current because of the impedance of the battery module, as shown in Fig. 2. This internal impedance estimation method works under the steady state of the battery, so we adopt the linear model shown in Fig. 3(b) in this article. The impedance of the battery (Z) during the steady state can be considered purely resistive [25]. The battery impedance can be calculated by (4), where $v_{b\max}$, $v_{b\min}$, $i_{b\max}$, and $i_{b\min}$ represent the maximums and minimums of the instantaneous value of the battery module current and voltage in one ripple cycle

$$Z = \frac{\Delta v_b}{\Delta i_b} = \frac{|v_{b\max} - v_{b\min}|}{|i_{b\max} - i_{b\min}|}. \tag{4}$$

Step 2: Estimate the battery module's OCV. Fig. 3(b) shows the linear battery model adopted in this article, where I_b and V_b represent the average values of the battery module voltage and current during a pulsation cycle, respectively. I_b is negative during discharging and positive during charging. Thus, the OCV can be estimated by the following equation:

$$\mathrm{OCV} = V_b - I_b \cdot Z. \tag{5}$$

Step 3: Estimate the SOC from a precharacterized and predefined OCV-SOC lookup table (LUT) for each battery module once the OCV is confirmed. There is a one-to-one correspondence between OCV and SOC.

Step 4: Estimate the effective capacity (Q_e) of the battery module. Two accurate SOC values and the integrated current between these two values are sufficient to estimate the capacity of the battery cell. When the OCV changes from OCV_0 to OCV_t, the SOC does from SOC_0 to SOC_t. Since the OCV versus SOC curve is monotone, it can be inverted, and therefore the SOC of a battery module can be estimated using a OCV-SOC LUT and the measured OCV. Then the effective capacity can be calculated from (6), where i_b represents the instantaneous value of the battery module current

$$\mathrm{SOC}_t = \mathrm{SOC}_0 + \frac{\int_0^t i_b dt}{Q_e} \Rightarrow Q_e = \frac{\int_0^t i_b dt}{\mathrm{SOC}_t - \mathrm{SOC}_0}. \tag{6}$$

The unbalance in the grid voltage or lines impedance would affect the estimation of the parameters. In this case, there will be negative sequence current in the system, which may bring distortions to the battery currents. To solve this problem, a negative-sequence grid voltage feedforward control can be applied. In this way, the CHBC can actively produce an amount of negative-sequence voltage in response to system voltage imbalance, thereby suppressing the negative-sequence current resulting from the system voltage imbalance. Then, the imbalance voltage's impact on the estimation of the battery parameters can be eliminated.

A. *Testing Methods for the OCV-SOC Curve*

OCV test methods have been extensively studied by many researchers to get more reliable OCV-SOC curve and more precise lithium battery model [32]–[38]. In order to shorten the test time to the greatest extent, we adopt the constant current discharging/charging with a short intermission method [32], [33] in this article. When the test starts, the battery is fully charged or discharged and left at rest for 1 h. An SOC interval (ΔSOC) of 1% is obtained by 0.5C (5 A) constant current discharging/charging, followed by a pause of 1 min, which is aimed at making the battery module voltage approximate OCV conditions [32], [33]. Repeat in this way until the cut-off voltage of the battery module, i.e., 18 V, is reached or the battery is fully charged after a constant voltage phase is applied. OCV is the average value of the voltages measured after a pause during processes of charging and discharging. The whole test carried out at 25 °C takes only several hours [32], [33].

Polynomial function is usually used to fit the OCV-SOC curve, which can be programmed in the actual control system then. Unfortunately, ill-conditioned curve with low reliability and resolution can be easily caused by polynomial fitting. Hence, we design a 2 × 101 LUT with an SOC interval of 1%. A monotone, nonlinear interpolation of OCV values is required to get the intermediate values between two data points in order to get the OCV curve with a higher resolution. We propose using piecewise cubic Hermite polynomials, which preserves the

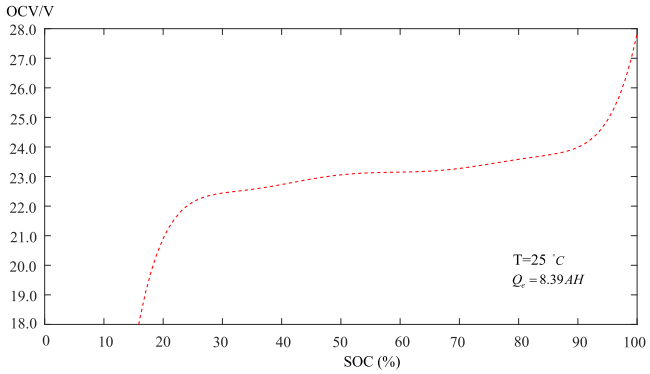

Fig. 4. OCV-SOC curve obtained by piecewise cubic Hermite polynomials interpolation.

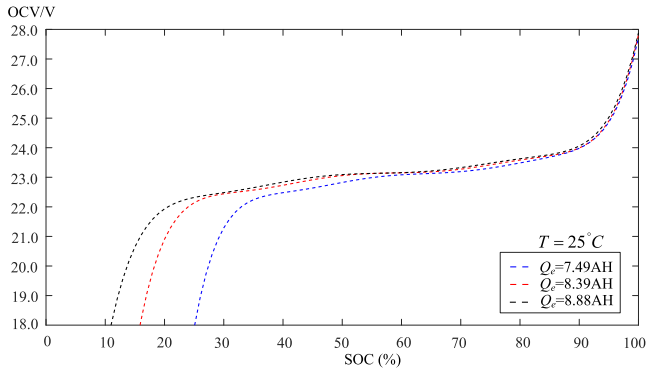

Fig. 5. OCV-SOC curves under different effective capacity.

shape of the data, visually pleasing, and respects monotonicity, for the interpolation of OCV values [34]. The OCV-SOC curve obtained by piecewise cubic Hermite polynomials interpolation is shown in Fig. 4, where the SOC is defined according to the nominal capacity.

B. Normalization of the OCV-SOC Curve

In practical application, the nominal capacity is usually used to perform the SOC estimation rather than the effective capacity. However, the accuracy of SOC estimation cannot be guaranteed because the effective capacity gradually degrades while the cycle time is increasing. Taking a battery module with a rated capacity of 10 Ah and a 20% capacity degradation as an example, the SOC should be zero after the fully charged battery completely discharges. However, if the capacity degradation is neglected, the SOC is 20%. Considerable error is introduced in SOC estimation, which would lead to overdischarge of the battery. Different OCV-SOC curves under different effective capacity tested at 25 °C and obtained by piecewise cubic Hermite polynomials interpolation are shown in Fig. 5, where the SOC is defined according to the nominal capacity. The significant differences of the OCV-SOC curves in Fig. 5 are caused by the different effective capacity. To address the above-mentioned problem, we propose normalizing the OCV-SOC curve. To accomplish this, the SOC is redefined as the ratio of the remaining capacity to the effective capacity, as shown by (7), where Q_r and Q_e represent

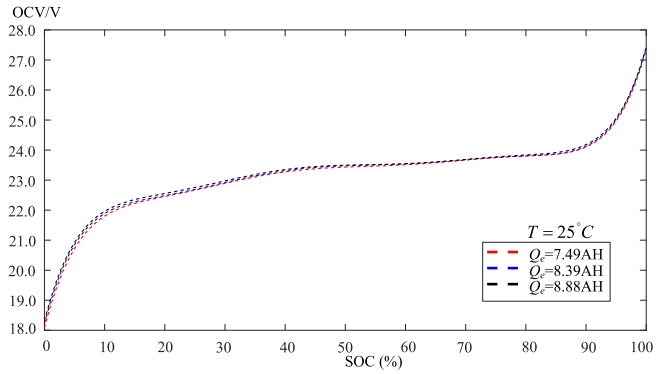

Fig. 6. OCV-SOC curve under different effective capacity after normalization.

remaining capacity and effective capacity of the battery module, respectively. The coulomb counting expression is also modified accordingly, shown as follows:

$$\mathrm{SOC} = \frac{Q_r}{Q_e} \times 100\% \tag{7}$$

$$\mathrm{SOC}_t = \mathrm{SOC}_0 + \frac{\int_0^t i_b dt}{Q_e}. \tag{8}$$

We adopt the normalization method described above to normalize the OCV-SOC curves in Fig. 5. Fig. 6 gives a clear illustration of the normalized OCV-SOC curves. The OCV-SOC curves arrive at a mutually agreed-upon state though they are tested under different effective capacity, which is a verification for the validity of the normalization method. The second-life battery module's OCV-SOC curves under arbitrary condition can be obtained by only one OCV-SOC test under certain effective capacity with the adoption of the proposed normalization method.

Based on the above-mentioned work, we can acquire accurate online estimations of effective capacity, internal impedance, OCV, and SOC of a second-life battery module following the steps 1–4 aforementioned.

IV. Distributed Power Sharing Strategy of Power Modules in CHBC-SLBESS

Compared with the new ones, the second-life battery modules tend to react in different way according to their significantly different parameters, such as effective capacity, SOC, and voltage. So, the traditional SOC (defined according to nominal capacity) balancing control strategy reported in [25], which is aimed at increasing utilization of the new battery's capacity, is not applicable in CHBC-SLBESS. To address this issue, a distributed power sharing strategy among the power modules in CHBC-SLBESS is proposed, which includes both the interphase power sharing strategy and the interbridge power sharing strategy.

The proposed distributed power sharing strategy is based on the interphase power sharing weighting factor ω_k and the interbridge power sharing weighting factor ω_{kj}, which can represent the status (current effective capacity, SOC and voltage) of

the applied second-life battery modules. The interbridge power sharing weighting factor (ω_{kj}) of the *j*th power module of phase *k* and interphase power sharing weighting factor (ω_k) of phase *k* can be derived from (9) and (10), respectively, where Q_{ekj}, SOC_{kj}, and V_{bkj} represent the effective capacity, instantaneous SOC, and average battery voltage during a pulsation cycle of the *j*th power module of phase *k*. It is worth noting that the weighting factor during discharging is different from that during charging. Based on the interphase and interbridge power sharing weighting factor, the sharing power of each phase P_k^* and the sharing power of each power module P_{kj}^* can be calculated by (11) and (12), respectively, where P^* represents the total reference active power of the system

$$\omega_{kj} = \begin{cases} \dfrac{Q_{ekj}\cdot \mathrm{SOC}_{kj}\cdot V_{bkj}}{\sum_{j=1}^{n} Q_{ekj}\cdot \mathrm{SOC}_{kj}\cdot V_{bkj}} & \text{discharging} \\ \dfrac{Q_{ekj}\cdot (1-\mathrm{SOC}_{kj})\cdot V_{bkj}}{\sum_{j=1}^{n} Q_{ekj}\cdot (1-\mathrm{SOC}_{kj})\cdot V_{bkj}} & \text{charging} \end{cases} \tag{9}$$

$$\omega_{k} = \begin{cases} \dfrac{\sum_{j=1}^{n} Q_{ekj}\cdot \mathrm{SOC}_{kj}\cdot V_{bkj}}{\sum_{k}\sum_{j=1}^{n} Q_{ekj}\cdot \mathrm{SOC}_{kj}\cdot V_{bkj}} & \text{discharging} \\ \dfrac{\sum_{j=1}^{n} Q_{ekj}\cdot (1-\mathrm{SOC}_{kj})\cdot V_{bkj}}{\sum_{k}\sum_{j=1}^{n} Q_{ekj}\cdot (1-\mathrm{SOC}_{kj})\cdot V_{bkj}} & \text{charging} \end{cases} \tag{10}$$

$$P_k^* = \omega_k \cdot P^* \tag{11}$$

$$P_{kj}^* = \frac{\omega_{kj} P^*}{3}. \tag{12}$$

To make full utilization of the battery capacity, each of the applied battery modules will charge/discharge at different rates according to their characteristics. This adopted distributed power sharing strategy ensures that the charging/discharging trajectories of all the applied second-life battery modules during a discharging/charging cycle will all arrive at their minimum/maximum values at the same time. The average battery current during a pulsation cycle of the *j*th power module of phase *k*, i.e., I_{bkj}, should satisfy the following equation:

$$\frac{I_{bk1}}{\omega_{k1}} = \frac{I_{bk2}}{\omega_{k2}} = \cdots = \frac{I_{bkn}}{\omega_{kn}}. \tag{13}$$

Meanwhile, the interphase power sharing weighting factors satisfy the following equation:

$$\omega_a + \omega_b + \omega_c = 1. \tag{14}$$

V. Differentiation Power Control Strategy of Modules in CHBC-SLBESS

A differentiation power control strategy of CHBC-SLBESS is proposed in this paper, whose overall control structure is shown in Fig. 7. The whole strategy consists of the following five parts:

1) online parameter estimation of the second-life battery module;
2) distributed power sharing strategy;
3) decoupled current control of CHBC;
4) interbridge differentiation power control strategy;
5) interphase differentiation power control strategy.

We have respectively described the first two parts of this strategy in Sections III and IV in detail and will not reiterate them here. The third part, i.e., decoupled current control, just as described in [39], will not be detailed here either. The reference of the output positive sequence fundamental voltage of CHBC, i.e., v_a^+, v_b^+, and v_c^+, can be obtained by applying the inverse *dq* transformation to the following equation:

$$\begin{bmatrix} v_d \\ v_q \end{bmatrix} = \begin{bmatrix} v_{sd} \\ v_{sq} \end{bmatrix} - \begin{bmatrix} 0 & -\omega L_s \\ \omega L_s & 0 \end{bmatrix} \begin{bmatrix} i_d \\ i_q \end{bmatrix} - K_{P,i} \begin{bmatrix} i_d^* - i_d \\ i_q^* - i_q \end{bmatrix} - K_{i,i} \int \begin{bmatrix} i_d^* - i_d \\ i_q^* - i_q \end{bmatrix} dt \tag{15}$$

where v_d and v_q are the *d*- and *q*-axis positive-sequence components of the converter's output voltage, whereas i_d and i_q are those of the grid current, respectively. We assumed that the grid voltage is balanced and only positive-sequence component exists in it, so the grid current is also balanced. v_{sd} and v_{sq} are the *d*- and *q*-axis positive-sequence components of the grid voltage, respectively. i_d^* and i_q^* are the given *d*- and *q*-axis current commands. $K_{P,i}$ and $K_{i,i}$ are the parameters of the current controller. The tuning process of the current loop controller can be seen in the Appendix. After being decoupled, the *d*- and *q*-axis currents can be controlled independently and the frequency domain models of converter with control in *d*- and *q*-axis are the same. We select the *d*-axis as the active power axis. So the selection of the weighting factor for charging and discharging depends on the sign of i_d^*, which indicates the phase of grid side current with respect to the grid voltage. Hence, we use the sign of i_d^* to perform the dynamic changeover through an edge detector in this strategy.

The fourth and fifth parts play a crucial role in the proposed differentiation power control strategy, which will be detailed in this chapter.

A. Interbridge Differentiation Power Control Strategy

The aim of the interbridge differentiation power control strategy is to control the power of the series-connected power modules in the same phase independently according to the applied second-life battery modules' characteristics. To realize the independent power control of the power modules in the same phase, each of the applied battery modules will charge/discharge at different rates, which can promise full utilization of the battery capacity. However, when *n* power modules are series-connected as shown in Fig. 1, the power transfer management is not really independent due to the fact that the current flowing through them is the same and the ac current in this case is controlled through the combined action of the *n* power modules. The challenging independent power control of the series-connected power modules has been proven to be strictly related to stability problems [40]–[42]. In summary, stability problems arise because $n + 1$ state variables (one ac current plus *n* modules' power) are managed with only *n* switching functions [43].

To resolve this problem, we introduce $n - 1$ closed module power control loops for the second to the *n*th power module in each phase. The reference of the closed module power control loop can be obtained by (12). The module power controller selects the amplitude $(\overset{\Lambda}{S}_{kj}^+)$ for the positive-sequence fundamental component (S_{kj}^+) of the switching function (S_{kj}). The phase of S_{kj}^+ is the same with that of the positive-sequence fundamental

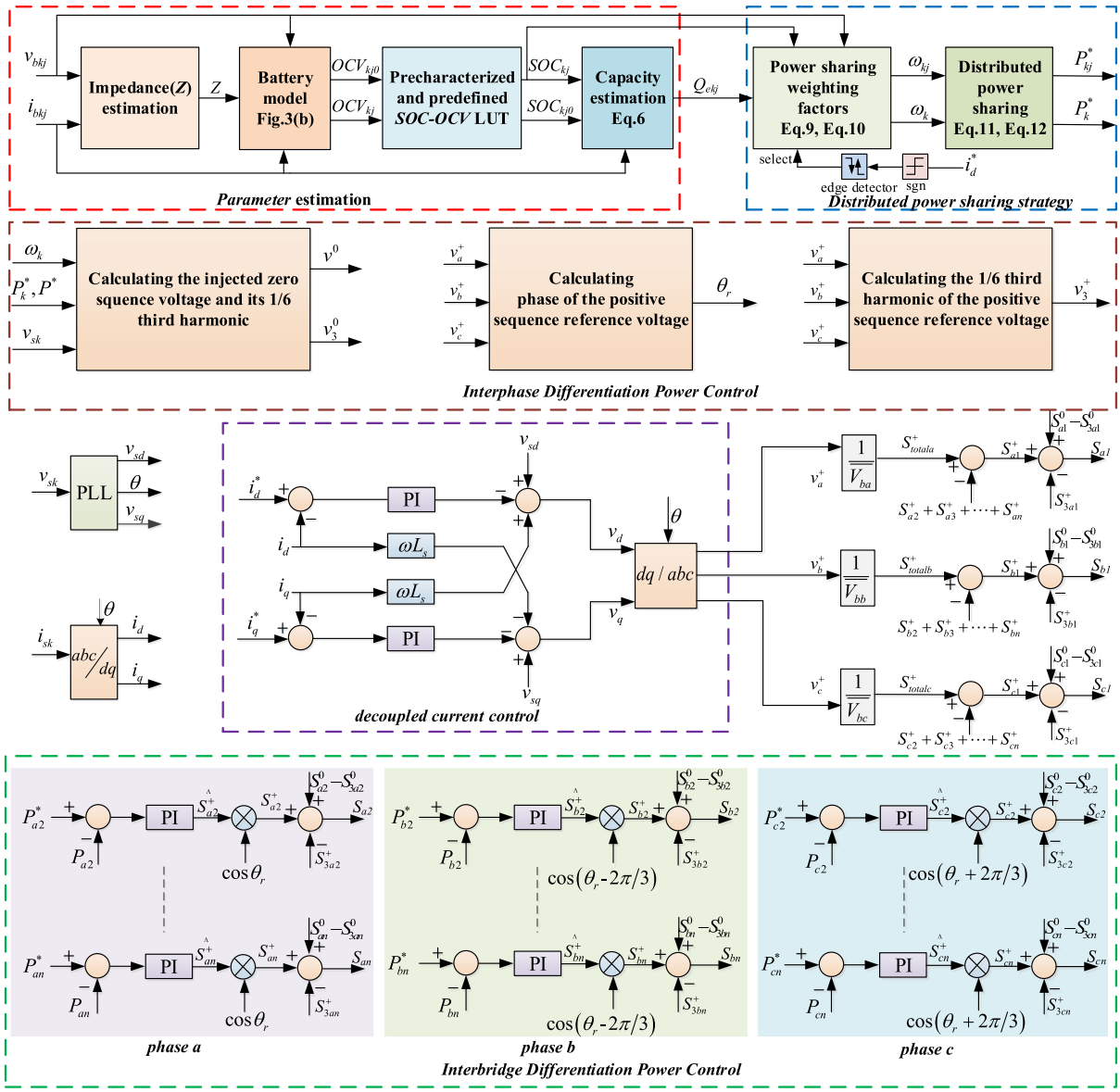

Fig. 7. Overall control structure of the proposed differentiation power control strategy.

component of the converter output voltage, i.e., θ_r. The reference of positive-sequence fundamental component of the converter output voltage, i.e., v_k^+, can be obtained by decoupled current control in the *dq* synchronous rotating frame. v_k^+ divided by $\overline{V_{bk}}$, which represents the average voltage of the battery modules in one phase, is the positive-sequence fundamental component of total modulation wave for each phase, i.e., S_{totalk}^+. When we obtain the positive-sequence fundamental components of the switching functions for the second to the *n*th power module, the positive-sequence fundamental component of switching function for the first module in each phase can be obtained by the following equation:

$$S_{k1}^+ = S_{\text{totalk}}^+ - \left(S_{k2}^+ + \cdots + S_{kn}^+\right). \tag{16}$$

This proposed interbridge differentiation power control strategy can not only realize independent power control of the power modules in the same phase, but also avoid instability problem.

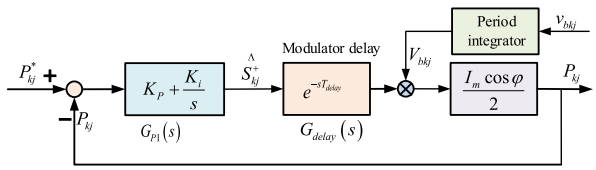

Fig. 8. Block diagram of the introduced closed module power control loop in frequency domain.

The block diagram of the introduced closed module power control loop in frequency domain is shown in Fig. 8, where I_m represents the amplitude of the grid current and φ represents the phase difference between the grid current and positive-sequence fundamental component of the converter output voltage.

As previously mentioned, a second harmonic component exists in the battery voltage, which would lead to the third harmonic component in the grid current. To restrain the third harmonic

component in grid current, we adopt a whole period integrator, as shown in Fig. 8. The third harmonic component is eliminated from the grid current in this way. The whole period integrator can be described as follows:

$$V_{bkj} = \frac{1}{T} \cdot \int_{t}^{t+T} v_{bkj} dt. \tag{17}$$

The total system delay can be considered as an approximate equivalent of the half of the switching period $T_{\rm sw}/2$, i.e.

$$G_{\rm delay}(s) = e^{-sT_{\rm delay}} \approx \frac{1}{1 + s \cdot T_{\rm sw}/2}. \tag{18}$$

The open-loop transfer function is then given by the following equation:

$$G_{\rm open}(s) = \frac{K_P \cdot s + K_i}{s} \cdot \frac{1}{1 + s \cdot T_{\rm sw}/2} \cdot \frac{V_{bkj} \cdot I_m \cdot \cos\varphi}{2}. \tag{19}$$

The PI module power controller is designed by zero-pole cancellation method. The response time of the closed module power control loop has to be in accordance with that of the current loop in order to guarantee the good dynamic performance of the system. Then, the PI parameters of the module power controller, i.e., K_P and K_i, can be figured out.

B. Interphase Differentiation Power Control Strategy

In addition to the battery parameter inconsistency among the battery modules in the same phase, battery parameter inconsistency among different phases, like the inconsistent total effective capacity of each phase, should not be neglected in order to make full utilization of all the applied battery modules' capacity. In this case, each phase should assume the different amount of power according to its specific battery configuration. If not, the battery modules of certain one phase would be the first to arrive the cut-off states, which would result in underutilization of effective capacity of the battery modules in the other two phases simultaneously. To address the above-mentioned issue, the interphase differentiation power control strategy was proposed, which can redistribute the power of each phase according to the applied battery modules' characteristics in real time. The power assumed by each phase can be calculated by (11).

The interphase differentiation power control strategy is implemented by injecting a zero-sequence fundamental frequency voltage into the converter output voltage. The injection of zero-sequence voltage would not lead to introduction of the zero-sequence current because of the star configuration of CHBC-SLBESS. Therefore, the FFZSVI method redistributes the power among three phases as required to provide three-phase balanced currents. With the introduction of this fundamental frequency zero-sequence voltage v^0, as shown in (20), the converter voltage reference v_k can be rewritten as (21). V_{0m} and θ_0 represent the amplitude and phase angle of the injected zero-sequence voltage

$$v^0 = V_{0m} \cos(\omega t + \theta_0) \tag{20}$$

$$v_k = v_k^+ + v^0. \tag{21}$$

The power redistribution caused by the injected zero-sequence voltage for each phase can be expressed by (22), where φ_{ia} represents the phase angle of the A phase current and ΔP_k should satisfy (23). No additional active power is produced after the injection of zero-sequence voltage, but the power distribution among three phases is changed.

The amplitude and phase angle of the injected zero-sequence voltage can be figured out according to (22), as shown by (24) and (25), respectively. V_g represents the rms value of line voltage

$$\begin{cases} \Delta P_a = \frac{1}{2} V_{0m} I_m \cos(\theta_0 - \varphi_{ia}) = P^* \left(\omega_a - \frac{1}{3}\right) \\ \Delta P_b = \frac{1}{2} V_{0m} I_m \cos(\theta_0 - \varphi_{ia} + \frac{2\pi}{3}) = P^* \left(\omega_b - \frac{1}{3}\right) \\ \Delta P_c = \frac{1}{2} V_{0m} I_m \cos\left(\theta_0 - \varphi_{ia} - \frac{2\pi}{3}\right) = P^* \left(\frac{2}{3} - \omega_b - \omega_a\right) \end{cases} \tag{22}$$

$$\Delta P_a + \Delta P_b + \Delta P_c = 0 \tag{23}$$

$$\begin{aligned} V_{0m} &= \frac{4\,|P^*|}{\sqrt{3} I_m} \sqrt{\omega_a^2 + \omega_b^2 + \omega_a \omega_b - \omega_a - \omega_b + \frac{1}{3}} \\ &= 2\sqrt{2} V_g \sqrt{\omega_a^2 + \omega_b^2 + \omega_a \omega_b - \omega_a - \omega_b + \frac{1}{3}} \end{aligned} \tag{24}$$

$$\theta_0 = a\,\tan 2(1 - 2\omega_b - \omega_a, \sqrt{3} \cdot \omega_a - \sqrt{3}/3) + \varphi_{ia}. \tag{25}$$

When the FFZSVI is put into practice, the zero-sequence voltage superimposed on the reference voltage of each module is gained by multiplying v^0 and ω_{kj}. Then the fundamental frequency zero-sequence component of the switching function, i.e., S_{kj}^0, can be obtained. The switching function of each module is the sum of S_{kj}^0 and S_{kj}^+, as shown by the following equation:

$$S_{kj} = S_{kj}^+ + \frac{\omega_{kj} \cdot v^0}{V_{bkj}} = S_{kj}^+ + S_{kj}^0. \tag{26}$$

However, the injection of the fundamental frequency zero-sequence component comes at the expense of increasing converter output voltages. While the converter output voltages increase with the severity of the battery parameter inconsistency and reach the limit set by the dc-side second-life battery module voltages, the target of delivering balanced grid currents with the FFZSVI method fails. To avoid the overmodulation, we must ensure that the maximum value of converter output voltages should be less than the sum of the battery module voltages in one phase. The injected zero-sequence voltage is different from that in [25], where the injected zero-sequence voltage is related to the SOC of each phase and would change with SOC during the SOC balancing process. In contrast, the injected zero-sequence voltage in this article is related to interphase power sharing weighting factor, which depends on the battery parameters and is nearly invariable during a charging/discharging cycle. So, the injected zero-sequence voltage in this article can also be considered nearly invariable. To guarantee no overmodulation during the whole charging/discharging cycle after the injection of zero-sequence voltage, the converter output voltage v_k should satisfy formula (27), where $V_{bkj\,\min}$ is the minimum value of battery voltage during the whole charging/discharging cycle

$$\max\{v_a, v_b, v_c\} \le \sum_{j=1}^{n} V_{bkj\,\min}. \tag{27}$$

An SOC window between 5% and 95% is used in the actual system for battery safety because error exists in the estimation

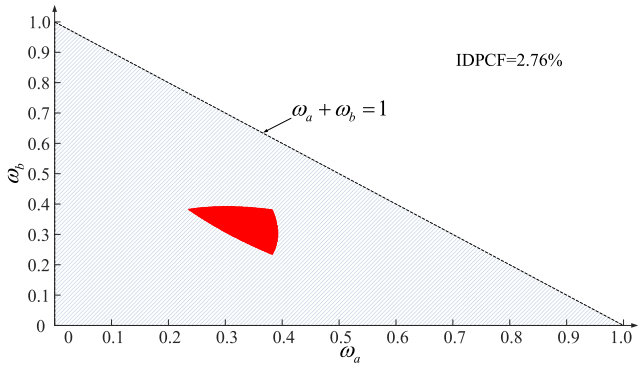

Fig. 9. Control range of the interphase differentiation power control strategy based on FFZSVI.

of SOC. High equivalent switching frequency ask for a small filter inductance in CHBC, then the voltage of the filter inductance can be ignored. In this way, the converter output voltage v_k can be shown as follows:

$$v_k = v_{sk} + v^0. \tag{28}$$

After the reasonable approximation, the maximum value of converter output voltage can be indicated as a function of ω_a and ω_b, i.e., $\max\{v_a, v_b, v_c\}(\omega_a, \omega_b)$. The theoretical range of ω_a and ω_b is (0, 1). This article also provides a quantitative analysis method for the interphase differentiation power control capability, which offers a reference for the battery configuration and design of fault-tolerant control strategy in CHBC-SLBESS. Interphase differentiation power control capability is defined as the ability of dealing with interphase battery parameter inconsistency. All possible interphase battery parameter inconsistency cases fall within a shaded triangle and can be represented by a unique operation point (ω_a, ω_b) inside the shaded triangle, as shown in Fig. 9. The coordinates of all the points inside the shaded triangle simultaneously satisfy the following inequalities: $0 < \omega_a < 1$, $0 < \omega_b < 1$, and $\omega_a + \omega_b < 1$. If the maximum converter output voltage satisfies (27), then three-phase balanced grid currents can be generated without overmodulation, and this operation point is in the control range of the given method. All operation points in the control range form a two-dimensional space, defined as interphase differentiation power control space (IDPCS). The ratio of the area of IDPCS (S_{IDPCS}) to the area of the shaded triangle (S_{trangle}) is defined as the interphase differentiation power control factor (IDPCF)

$$\text{IDPCF} = \frac{S_{\text{IDPCS}}}{S_{\text{trangle}}} = \frac{\int_0^1 \int_0^1 F(\omega_a, \omega_b)\, d_{\omega_a} d_{\omega_b}}{S_{\text{trangle}}} \tag{29}$$

where $F(\omega_a, \omega_b)$ is defined as follows:

$$F(\omega_a, \omega_b) = \begin{cases} 0, & \max\{v_a, v_b, v_c\}(\omega_a, \omega_b) > \sum_{j=1}^{n} V_{bkj\,\min} \\ 1 & \max\{v_a, v_b, v_c\}(\omega_a, \omega_b) \le \sum_{j=1}^{n} V_{bkj\,\min}. \end{cases} \tag{30}$$

TABLE II
MAIN PARAMETERS OF THE PROPOSED CHBC-SLBESS

Parameters	Values
Grid line voltage	175 V
Rated power	10 kW
Cascade number	8
Rated voltage of battery module	23 V
DC capacitor	11 mF
Grid side filter inductance	0.5 mH
Switching frequency	1 kHz

The proposed quantitative analysis method is used to quantify the control range of the interphase differentiation power control strategy based on FFZSVI. The system parameters shown in Table II are adopted. The analysis result is shown in Fig. 9, where the red section represents the IDPCS and the IDPCF is 2.76%.

As Fig. 9 shows, the control range of FFZSVI is very small because of the low utilization of the dc-side voltage. So overmodulation is prone to arise. Moreover, each of these applied battery modules will charge/discharge at different rates according to their characteristics, in order to all arrive at their maximum/minimum values at the same time. When the battery modules with significantly different parameters are applied in the same phase, there is a possibility that the amplitudes of switching functions for some modules are nearly closed to 1 or even more than 1 before the injection of zero-sequence voltage. In this case, overmodulation is more prone to arise after the injection of zero-sequence voltage. We can draw the conclusion that the interbridge differentiation power control strategy further narrows the control range of the interphase differentiation power control strategy based on FFZSVI under some certain cases.

Therefore, it is necessary to find a way to expand the control range of the differentiation power control strategy. Third harmonic injection is an effective way to improve the dc voltage utilization of the three-phase voltage-source converter [44]–[46]. Adding high-order harmonics to FFZSVI will not affect its power redistribution effort, since these harmonics are expected to generate zero average active power with the fundamental frequency grid currents. For symmetrical converter output voltages, a third harmonic injection with an amplitude of 1/6 of the fundamental frequency component achieves the highest ac output voltage without overmodulation. Having noted that the injected fundamental frequency zero-sequence voltage is also sinusoidal, a straightforward way to find a harmonic injection is to combine the optimal injection of the positive sequence with the optimal one of the zero sequence [44]. The method is hence named as the DTHVI method. The converter output voltage of phase *k* with DTHVI can be written as follows:

$$\begin{aligned} v_k &= v_k^+ - v_{3k}^+ + v^0 - v_3^0 \\ &= V_{+km}\cos(\omega t + \phi_k) - \frac{V_{+km}}{6}\cos(3\omega t + 3\phi_k) \\ &\quad + V_{0m}\cos(\omega t + \theta_0) - \frac{V_{0m}}{6}\cos(3\omega t + 3\theta_0) \end{aligned} \tag{31}$$

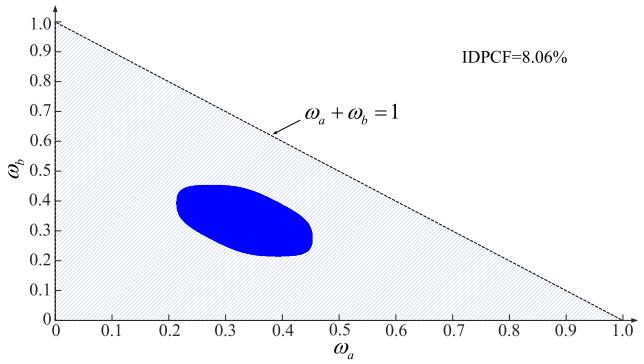

Fig. 10. Control range of the interphase differentiation power control strategy based on DTHVI.

where v_{3k}^{+} and v_3^0 represent the injected 1/6 third harmonic of the fundamental frequency positive-sequence component and the zero-sequence component of the converter output voltage, respectively. V_{+km} and ϕ_k represent the amplitude and phase angle of the fundamental frequency positive-sequence component of the converter output voltage, respectively. The interbridge power sharing weighting factor ω_{kj} is used as a standard to distribute the double third harmonics and the fundamental frequency zero-sequence voltage for each power module. Then, the switching function (S_{kj}) of each power module can be described as follows:

$$\begin{aligned} S_{kj} &= S_{kj}^{+} - S_{3kj}^{+} + S_{kj}^{0} - S_{3kj}^{0} \\ &= S_{kj}^{+} - \frac{\omega_{kj} \cdot v_3^{+}}{V_{bkj}} + \frac{\omega_{kj} \cdot v^{0}}{V_{bkj}} - \frac{\omega_{kj} \cdot v_3^{0}}{V_{bkj}} \end{aligned} \tag{32}$$

where S_{3kj}^{+} and S_{3kj}^{0} represent the third harmonic of the positive-sequence component and third harmonic of the zero-sequence component of the switching function, respectively.

The proposed quantitative analysis method is also used to quantify the control range of the interphase differentiation power control strategy based on DTHVI. The analysis result is shown in Fig. 10, where the blue section represents the IDPCS of the interphase differentiation power control strategy based on DTHVI and the corresponding IDPCF is 8.06%. Compared with FFZSVI, DTHVI has a much wider control range. DTHVI method increases about 15% in the dc voltage utilization by the injection of the double 1/6 third harmonic voltage, which means it can also increase about 15% in the control range of the interbridge differentiation power control strategy.

VI. Experimental Validation

A. Experiment Prototype

In order to verify the feasibility and effectiveness of the proposed differentiation power control strategy of modules in CHBC-SLBESS, a downscaled prototype is built in the laboratory. Table II lists the main parameters of the prototype. The battery modules retired from EVs are applied in this prototype, whose detail parameters have been shown earlier in Table I. The initial SOC and effective capacity of the applied second-life battery modules are shown in Table III. The switching frequency is selected as 1 kHz, so the equivalent switching frequency is 16 kHz when the carrier phase shifted modulation is adopted here. The battery module, power module, and control system structure of the prototype are shown in Fig. 11. A distributed control system is applied to implement the proposed differentiation power control strategy. The control system is composed of maincontroller, subcontrollers in power modules, sampleboard, and battery management system (BMS). A framework of DSP+FPGA is adopted both in the maincontroller and subcontroller. We summarize the main functions of the maincontroller as follows:

1) communicating with host computer and receiving active and reactive power instructions;
2) communicating with BMS through CAN bus and sending instructions to the battery modules;
3) reading sample information from FPGA and completing the main control arithmetic and the interphase differentiation power control strategy.

We summarize the main functions of the subcontroller as follows:

1) storing the precharacterized and predefined second-life battery module's OCV-SOC lookup table (LUT);
2) online battery parameter estimation, such as effective capacity, internal impedance and SOC of the battery module;
3) completing the interbridge differentiation power control strategy.

TABLE III
Initial SOC and Effective Capacity of the Applied Second-Life Battery Modules

No	Phase A		Phase B		Phase C	
	Q_e/AH	*SOC*	Q_e/AH	*SOC*	Q_e/AH	*SOC*
1	8.7	68%	7.3	62%	6.7	63%
2	8.7	60%	6.8	65%	7.4	55%
3	8.9	54%	6.5	61%	6.6	64%
4	8.3	67%	7.4	65%	7.2	65%
5	8.6	56%	6.9	66%	6.8	66%
6	9.0	61%	6.5	53%	6.9	69%
7	9.3	58%	7.5	67%	7.3	64%
8	8.4	70%	6.7	46%	6.9	58%

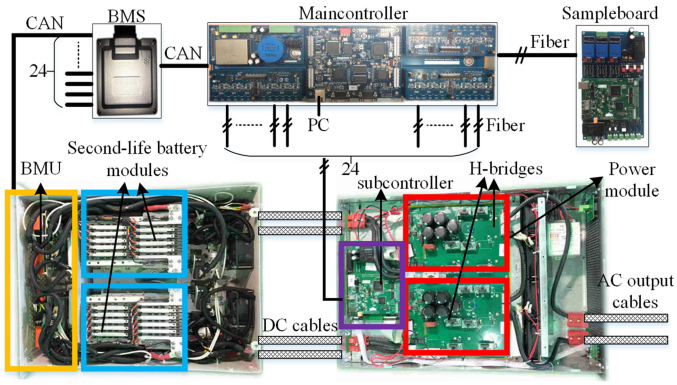

Fig. 11. Power module, battery module, and control system structure of the prototype of CHBC-SLBESS.

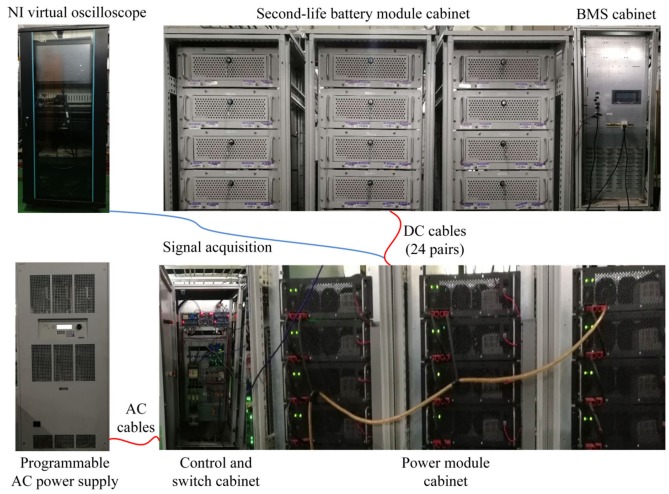

Fig. 12. Photograph of the experiment prototype.

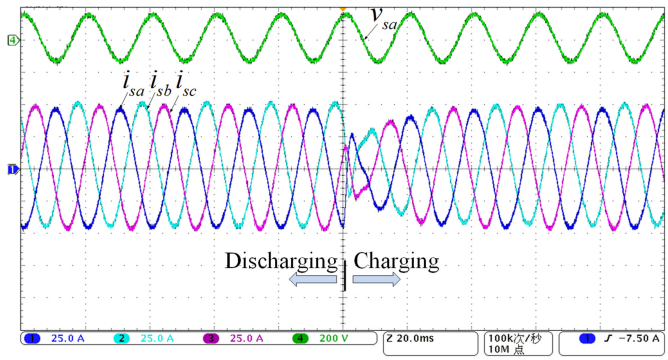

Fig. 13. Transient waveforms of the three-phase grid currents with FFZSVI-based interphase differentiation power control strategy.

The photo of the experiment prototype is shown in Fig. 12. The grid is simulated by RS90 programmable ac power supply. The battery current and voltage are measured and displayed by an NI virtual oscilloscope. Two power modules are contained in one power module cabinet and it is the same situation in one second-life battery module cabinet.

B. Validation of the Proposed Differentiation Power Control Strategy

As we can see from Table III, the effective capacity and SOC of the battery modules in the same phase are significantly different. Moreover, the total effective capacity of each phase, i.e., the sum of the effective capacity of all the battery modules in the same phase, is also significantly different. The transient waveforms of the grid currents and the converter output voltages from discharging to charging operation with a step change in rated active power from –10 to 10 kW at 0.12 s after the device is started under the proposed differentiation power control strategy are shown in Figs. 13 and 14. Here, the interphase differentiation power control strategy is implemented by FFZSVI first. Fig. 15 shows the waveforms of the switching functions for the power modules in phase A, where overmodulation arises because of

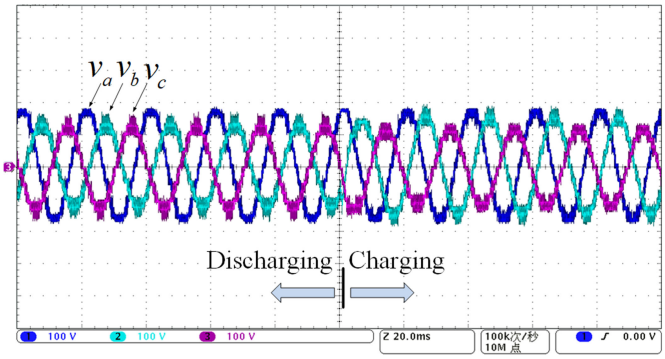

Fig. 14. Transient waveforms of the three-phase converter output voltages with FFZSVI-based interphase differentiation power control strategy.

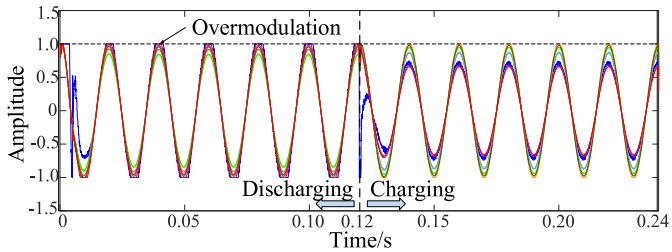

Fig. 15. Transient waveforms of the switching functions for the power modules in phase A with FFZSVI-based interphase differentiation power control strategy.

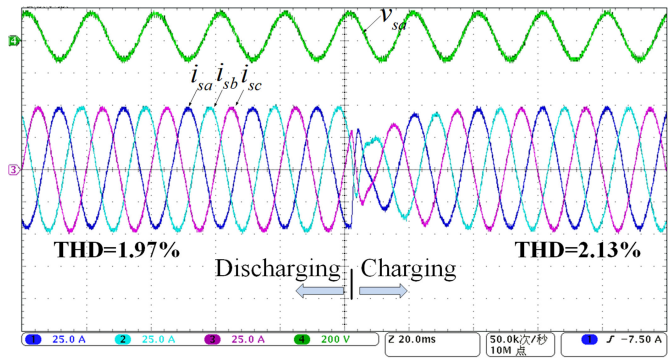

Fig. 16. Transient waveforms of the three-phase grid currents with DTHVI-based interphase differentiation power control strategy.

the significantly different battery parameters and narrow control range of FFZSVI described before. That is why the three-phase grid currents, shown in Fig. 13, are distorted and asymmetrical. Figs. 16 and 17 show the transient waveforms of the three-phase grid currents and the converter output voltages under the same experiment condition, but the only difference is that interphase differentiation power control strategy is implemented by DTHVI. Actually, the large distortion in the output voltage waves of CHBC arises from the injection of the third harmonic of the positive-sequence and zero-sequence fundamental frequency output voltage. However, the third harmonic injection would not introduce harmonic current in star-connected CHBC. The current total harmonic distortion (THD) is low (THD $<$ 5%), which can meet the grid code. So the distortion in the output

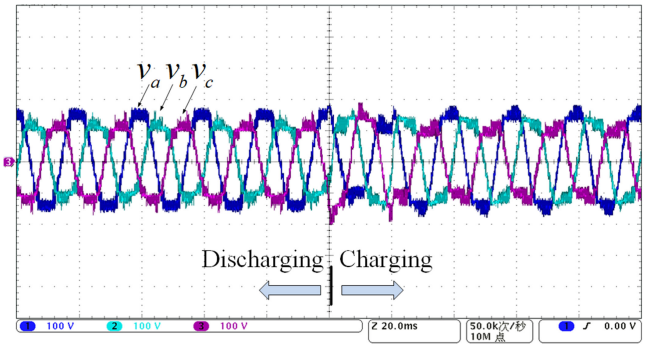

Fig. 17. Transient waveforms of the three-phase converter output voltages with DTHVI-based interphase differentiation power control strategy.

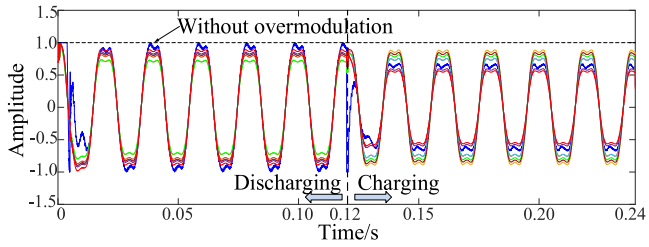

Fig. 18. Transient waveforms of the switching functions for the power modules in phase A with DTHVI-based interphase differentiation power control strategy.

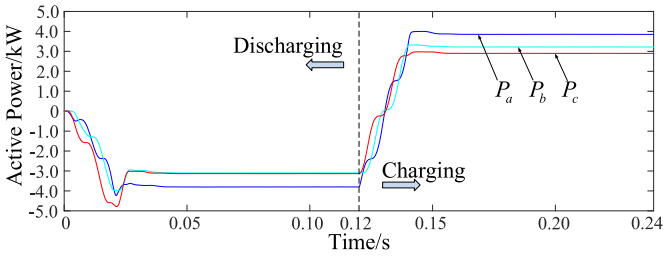

Fig. 19. Power distribution among three phases.

voltage of the CHBC does not have an impact on its connection to the grid. Fig. 18 shows the waveforms of the switching functions for the power modules in phase A at this moment, where overmodulation disappears because the control range of interphase differentiation power control strategy based on DTHVI is much wider than that based on FFZSVI. The three-phase grid currents are rebalanced, as shown in Fig. 16. So we adopt the DTHVI-based interphase differentiation power control strategy in this article. The three-phase converter output voltages shown in Fig. 17 are distorted and asymmetrical owing to the injection of the double third harmonics and the fundamental frequency zero-sequence component, respectively. Fig. 19 shows the power distribution among three phases under this case. The waveforms of the currents of the second-life battery modules in phase A are shown in Fig. 20. The conditions of the second-life battery modules in phase B and C are similar with that in phase A, which will not be displayed here. As we can see from Fig. 20, the battery modules in phase A charge and discharge at different rates according to their characteristics. When discharging, the

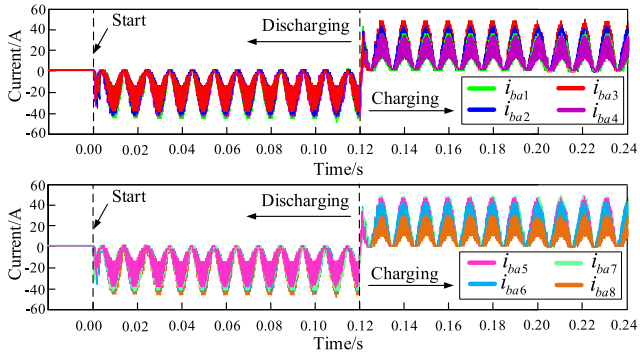

Fig. 20. Waveforms of the currents of the second-life battery modules in phase A.

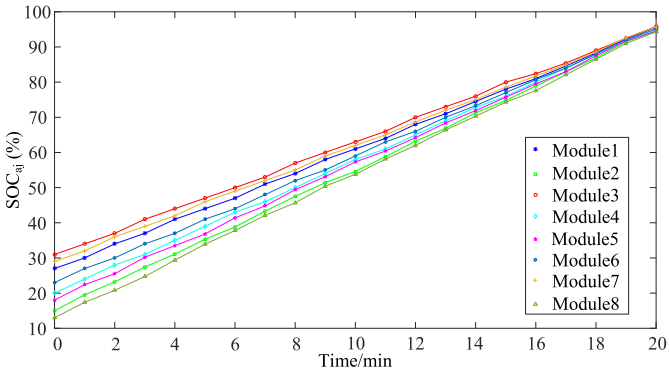

Fig. 21. SOC trajectories of the battery modules in phase A during charging.

average values of the battery currents during a pulsation cycle are $I_{ba1} = -22.98$ A, $I_{ba2} = -20.27$ A, $I_{ba3} = -18.60$ A, $I_{ba4} = -21.53$ A, $I_{ba5} = -18.73$ A, $I_{ba6} = -21.32$ A, $I_{ba7} = -20.90$ A, and $I_{ba8} = -22.68$ A. When charging, the average values of the battery currents during a pulsation cycle are $I_{ba1} = 17.60$ A, $I_{ba2} = 21.63$ A, $I_{ba3} = 24.78$ A, $I_{ba4} = 17.22$ A, $I_{ba5} = 23.73$ A, $I_{ba6} = 22.05$ A, $I_{ba7} = 24.36$ A, and $I_{ba8} = 15.75$ A. Then, we can draw the conclusion that the average values of the battery currents during a pulsation cycle satisfy (12) in both charge state and discharge state.

For validation of the full charging and discharging trajectory, all the second-life battery modules were started at different effective capacity, as shown in Table III, and different initial SOC, as shown in Figs. 21 and 22. The CHBC-SLBESS was running under the rated active power using the proposed differentiation power control strategy. The estimated SOCs of the battery modules in phase A are plotted during processes of charging and discharging, as shown in Figs. 21 and 22, respectively. A zero redefined SOC corresponds to the minimum capacity condition and a unity one corresponds to the fully charged condition after redefinition of it. We can see that the module with a lower initial SOC has a larger slope compared with the module with a higher SOC during charging and vice-versa during discharging. The SOCs of the battery modules in the same phase all arrive at their maximum/minimum values at around the same time using the proposed interbridge differentiation power control strategy. The SOC of each phase, i.e., SOC_k, is plotted during processes

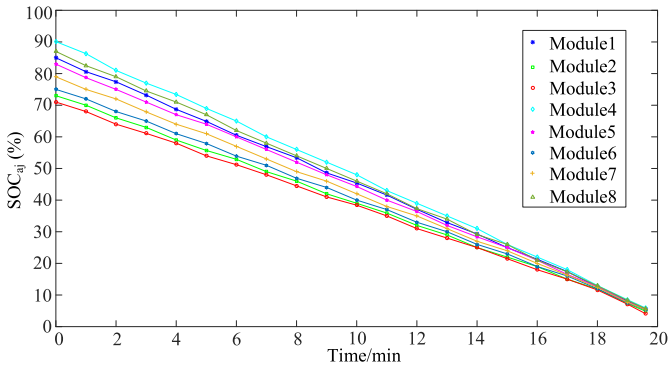

Fig. 22. SOC trajectories of the three phases during charging.

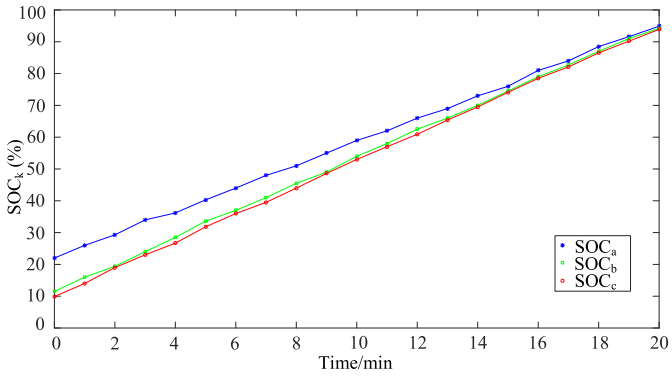

Fig. 23. SOC trajectories of the battery modules in phase A during discharging.

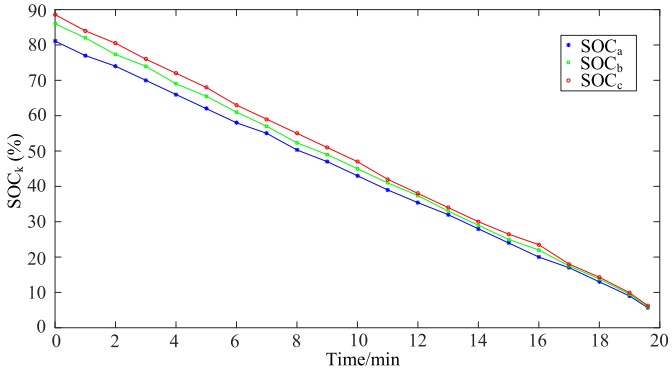

Fig. 24. SOC trajectories of the three phases during discharging.

of charging and discharging, as shown in Figs. 23 and 24, respectively. The SOC of each phase is defined by (33), rather than the mean value of the SOCs of all the battery modules in the same phase, as described in the following equation [25]:

$$\mathrm{SOC}_k = \frac{\sum_{j=1}^{n} Q_{ekj} \cdot \mathrm{SOC}_{kj}}{\sum_{j=1}^{n} Q_{ekj}}. \tag{33}$$

The SOCs of the three phases all arrive at their maximum/minimum values at around the same time using the proposed interphase differentiation power control strategy.

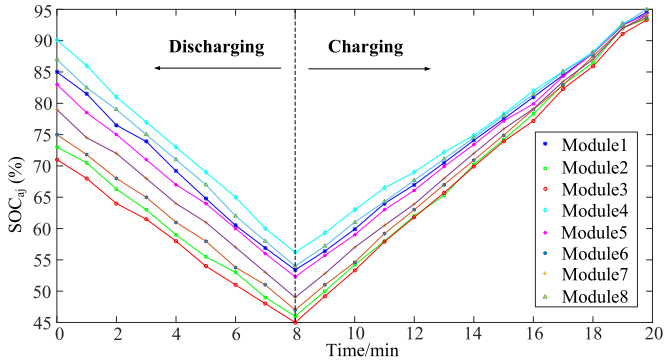

Fig. 25. Discharging–charging SOC trajectories of battery modules in phase A.

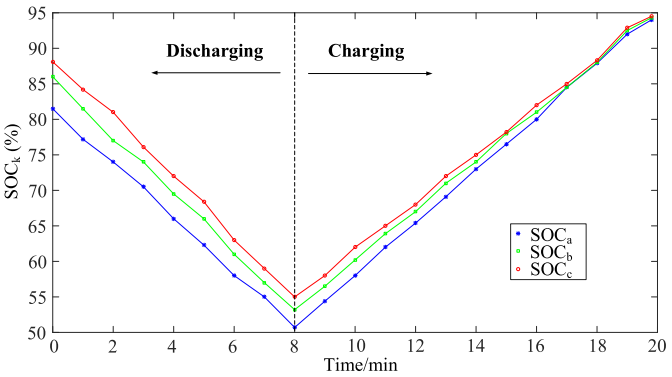

Fig. 26. Discharging–charging SOC trajectories of the three phases.

In order to find out the effect of load variation on the system, we have added SOC discharging–charging trajectories of the system, as shown in Figs. 25 and 26. We think that the system's switching from discharging mode to charging mode with the rated active power can represent the most dramatical load variation. Fig. 25 shows the experimental result of discharging–charging SOC trajectories of the battery modules in phase A when the converter was running with the rated active power. After 8 min, the converter switched from discharging mode to charging mode. Fig. 26 shows the experimental result of discharging–charging SOC trajectories of the three phases. As we can conclude from Figs. 25 and 26, though the mode of the converter changed during operation, the proposed differentiation power control strategy can also converge all modules to the same SOC whether they are in the same phase or different phases.

VII. Conclusion

A differentiation power control strategy for the power modules in CHBC-SLBESS has been proposed and analyzed to integrate the second-life battery modules with significantly different battery parameters suitably and to utilize them optimally. Moreover, a quantitative analysis method for the differentiation power control capability and a way to improve it are also proposed. This differentiation power control strategy redistributes the power of the three phases and the power of the modules in the same phase according to the interphase and interbridge power sharing

weighting factors, respectively, which depend on the second-life battery modules' characteristics, such as SOC, effective capacity and voltage. In this way, all of these applied battery modules, whether they are in the same phase or different phases, will charge/discharge at different rates and the discharging/charging trajectories of the battery modules during a discharging/charging cycle will all arrive at their minimum/maximum values simultaneously. The underutilization of effective capacity, overcharge and overdischarge of the battery modules can be avoided. Finally, the superior performance of CHBC-SLBESS and the feasibility of the proposed differentiation power control strategy are demonstrated and verified by the experimental results.

APPENDIX

The Appendix shows the details about tuning process of the current loop controller and the module power loop controller.

The d- and q-axis components of current vector can be controlled independently after being decoupled and the frequency domain models of the converter with control in d- and q-axis are the same. The block diagram of d-axis current control in frequency domain is taken as an example, as shown in Fig. 27.

The equivalent gain of converter K_{PWM} is selected as 1. The normal delay in the system, which affects the stability of the system, is also taken into consideration for accurate analysis of the system. The open-loop transfer function of the current control loop is as follows:

$$\begin{aligned} G_i(s) &= G_{PI,i}(s)G_{\mathrm{delay}}(s)G_{\mathrm{plant}}(s) \\ &= \left(K_{P,i} + \frac{K_{i,i}}{s}\right)\left(e^{-sT_{\mathrm{delay}}}\right)\left(\frac{1}{R+sL_s}\right). \end{aligned} \tag{34}$$

The total system delay can be considered as an approximate equivalent of the half of the switching period $T_{\mathrm{sw}}/2$, i.e.

$$G_{\mathrm{delay}}(s) = e^{-sT_{\mathrm{delay}}} \approx \frac{1}{1 + s \cdot T_{sw}/2}. \tag{35}$$

When designing the PI parameter, the stability of the system is most important. In the Bode diagram, the phase margin should be in the range of 30° to 60° and the magnitude-frequency characteristic of open-loop function should cross 0 dB with a slope of –20 dB/dec. The design of the current loop PI controllers focuses on the selection of open-loop crossover frequency $f_{cr,i}$ and PI zero-turning frequency $f_{zt,i}$, which satisfy

$$\left\|G_i\left(j2\pi f_{cr,i}\right)\right\| = 1 \qquad f_{zt,i} = \frac{K_{i,i}}{2\pi K_{P,i}}. \tag{36}$$

Taking the two abovementioned principles into consideration, the open-loop crossover frequency $f_{cr,i}$ should be much less than the switching frequency f_{sw} and the PI zero-turning frequency $f_{zt,i}$ should be much less than $f_{cr,i}$. A typical group of $f_{cr,i}$ and $f_{zt,i}$ is

$$f_{cr,i} = \left(\frac{1}{20} \sim \frac{1}{10}\right) f_{\mathrm{sw}} \qquad f_{zt,i} = \left(\frac{1}{20} \sim \frac{1}{10}\right) f_{cr,i}. \tag{37}$$

We select $f_{cr,i}$ and $f_{zt,i}$ as follows:

$$f_{cr,i} = \frac{1}{10} f_{\mathrm{sw}} \qquad f_{zt,i} = \frac{1}{10} f_{cr,i}. \tag{38}$$

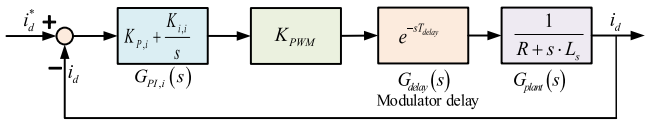

Fig. 27. Block diagram of d-axis current control in frequency domain.

The parasitic resistance R of the filter inductance L_s is estimated as 5% of the inductance impedance at fundamental frequency. Once the switching frequency is determined, the PI parameters of the current loop controller can be calculated as follows:

$$\begin{cases} K_{P,i} = \sqrt{\dfrac{\|R+j\omega_{cr,i}L_s\|^2}{1+\left(\frac{\omega_{zt,i}}{\omega_{cr,i}}\right)^2}} = \sqrt{\dfrac{(R)^2+(\omega_{cr,i}L_s)^2}{1+\left(\frac{\omega_{zt,i}}{\omega_{cr,i}}\right)^2}} \\ K_{i,i} = \omega_{zt,i}K_{P,i}. \end{cases} \tag{39}$$

The block diagram of the introduced closed module power control loop in frequency domain is shown in Fig. 8. The PI module power controller is designed by zero-pole cancellation method and the module power closed control loop is designed as a first-order system. The settling time of the closed module power control loop has to be in accordance with that of the current loop in order to guarantee the good dynamic performance of the system. Since the PI parameters of the current loop controller have been calculated out, the settling time of the current control loop can be obtained. Then, the PI parameters of the module power controller, i.e., K_p and K_i, can be figured out.

REFERENCES

[1] B. Kroposki *et al.*, "Achieving a 100% renewable grid: Operating electric power systems with extremely high levels of variable renewable energy," *IEEE Power Energy Mag.*, vol. 15, no. 2, pp. 61–73, Mar./Apr. 2017.

[2] M. Faisal, M. A. Hannan, P. J. Ker, A. Hussain, M. B. Mansor, and F. Blaabjerg, "Review of energy storage system technologies in microgrid applications: Issues and challenges," *IEEE Access*, vol. 6, pp. 35143–35164, 2018.

[3] V. A. Boicea, "Energy storage technologies: The past and the present," *Proc. IEEE*, vol. 102, no. 11, pp. 1777–1794, Nov. 2014.

[4] Y. Liu, W. Du, L. Xiao, H. Wang, S. Bu, and J. Cao, "Sizing a hybrid energy storage system for maintaining power balance of an isolated system with high penetration of wind generation," *IEEE Trans. Power Syst.*, vol. 31, no. 4, pp. 3267–3275, Jul. 2016.

[5] M. R. Sheibani, G. R. Yousefi, M. A. Latify, and S. Hacopian Dolatabadi, "Energy storage system expansion planning in power systems: A review," *IET Renewable Power Gener.*, vol. 12, no. 11, pp. 1203–1221, 2018.

[6] B. Dunn, H. Kamath, and J. M. Tarascon, "Electrical energy storage for the grid: A battery of choices," *Science*, vol. 334, no. 6058, pp. 928–935, 2011.

[7] H. P. Hellman *et al.*, "Benefits of battery energy storage system for system, market, and distribution network – case Helsinki," *CIRED, Open Access Proc. J.*, vol. 2017, no. 1, pp. 1588–1592, Oct. 2017.

[8] S. R. Deeba, R. Sharma, T. K. Saha, D. Chakraborty, and A. Thomas, "Evaluation of technical and financial benefits of battery-based energy storage systems in distribution networks," *IET Renewable Power Gener.*, vol. 10, no. 8, pp. 1149–1160, Sep. 2016.

[9] S. Mohan, A. Hooshmand, S. A. Pourmousavi, and R. Sharma, "BSS sizing and economic benefit analysis in grid-scale application," in *Proc. IEEE Power Energy Soc. Innovative Smart Grid Technol. Conf.*, Minneapolis, MN, USA, 2016, pp. 1–5.

[10] V. V. Viswanathan and M. Kintner-Meyer, "Second use of transportation batteries: Maximizing the value of batteries for transportation and grid services," *IEEE Trans. Veh. Technol.*, vol. 60, no. 7, pp. 2963–2970, Sep. 2011.

[11] G. Lacey, G. Putrus, and A. Salim, "The use of second life electric vehicle batteries for grid support," in *Proc. Eurocon*, Zagreb, Croatia, 2013, pp. 1255–1261.
[12] D. Strickland, L. Chittock, D. A. Stone, M. P. Foster, and B. Price, "Estimation of transportation battery second life for use in electricity grid systems," *IEEE Trans. Sustain. Energy*, vol. 5, no. 3, pp. 795–803, Jul. 2014.
[13] P. J. Hart, P. J. Kollmeyer, L. W. Juang, R. H. Lasseter, and T. M. Jahns, "Modeling of second-life batteries for use in a CERTS microgrid," in *Proc. Power Energy Conf. Illinois*, Champaign, IL, USA, 2014, pp. 1–8.
[14] M. Abdel-Monem, O. Hegazy, N. Omar, K. Trad, P. Van den Bossche, and J. Van Mierlo, "Lithium-ion batteries: Comprehensive technical analysis of second-life batteries for smart grid applications," in *Proc. 19th Eur. Conf. Power Electron. Appl.*, Warsaw, Poland, 2017, pp. P.1–P.16.
[15] D. T. Gladwin, C. R. Gould, D. A. Stone, and M. P. Foster, "Viability of "second-life" use of electric and hybridelectric vehicle battery packs," in *Proc. 39th Annu. Conf. IEEE Ind. Electron. Soc.*, Vienna, Austria, 2013, pp. 1922–1927.
[16] V. Calderaro, V. Galdi, G. Graber, F. Lamberti, and A. Piccolo, "A sizing method for economic assessment of II-life batteries for power system applications," in *Proc. IEEE Power Energy Soc. General Meeting*, Chicago, IL, USA, 2017, pp. 1–5.
[17] P. Cicconi, D. Landi, A. Morbidoni, and M. Germani, "Feasibility analysis of second life applications for Li-Ion cells used in electric powertrain using environmental indicators," in *Proc. IEEE Int. Energy Conf. Exhib.*, Florence, Italy, 2012, pp. 985–990.
[18] S. J. Tong *et al.*, "Off-grid photovoltaic vehicle charge using second life lithium batteries: An experimental and numerical investigation," *Appl. Energy*, vol. 104, no. 4, pp. 740–750, Apr. 2013.
[19] M. Aziz, T. Oda, T. Mitani, Y. Watanabe, and T. Kashiwagi, "Utilization of electric vehicles and their used batteries for peak-load shifting," *Energies*, vol. 8, no. 5, pp. 3720–3738, Apr. 2015.
[20] N. Mukherjee and D. Strickland, "Control of second-life hybrid battery energy storage system based on modular boost-multilevel buck converter," *IEEE Trans. Ind. Electron.*, vol. 62, no. 2, pp. 1034–1046, Feb. 2015.
[21] M. Abdel-Monem *et al.*, "Design and analysis of generic energy management strategy for controlling second-life battery systems in stationary applications," *Energies*, vol. 9, no. 11, pp. 889–913, Oct. 2016.
[22] N. Mukherjee, D. Strickland, A. Cross, and W. Hung, "Reliability estimation of second life battery system power electronic topologies for grid frequency response applications," in *Proc. 6th IET Int. Conf. Power Electron., Mach. Drives*, Bristol, U.K., 2012, pp. 1–6.
[23] J. I. Y. Ota, T. Sato, and H. Akagi, "Enhancement of performance, availability, and flexibility of a battery energy storage system based on a modular multilevel cascaded converter (MMCC-SSBC)," *IEEE Trans. Power Electron.*, vol. 31, no. 4, pp. 2791–2799, Apr. 2016.
[24] L. Maharjan, T. Yamagishi, and H. Akagi, "Active-Power control of individual converter cells for a battery energy storage system based on a multilevel cascade PWM converter," *IEEE Trans. Power Electron.*, vol. 27, no. 3, pp. 1099–1107, Mar. 2012.
[25] L. Maharjan, S. Inoue, H. Akagi, and J. Asakura, "State-of-Charge (SOC)-balancing control of a battery energy storage system based on a cascade PWM converter," *IEEE Trans. Power Electron.*, vol. 24, no. 6, pp. 1628–1636, Jun. 2009.
[26] L. Maharjan, T. Yamagishi, H. Akagi, and J. Asakura, "Fault-tolerant operation of a battery-energy-storage system based on a multilevel cascade PWM converter with star configuration," in *IEEE Trans. Power Electron.*, vol. 25, no. 9, pp. 2386–2396, Sep. 2010.
[27] D. Linden, *Linden's Handbook of Batteries*, 4th ed., T. B. Reddy, Ed., New York, NY, USA: McGraw-Hill, 2011.
[28] J. Li, M. Mazzola, J. Gafford, and N. Younan, "A new parameter estimation algorithm for an electrical analogue battery model," in *Proc. 27th Annu. IEEE Appl. Power Electron. Conf. Expo.*, Orlando, FL, USA, 2012, pp. 427–433.
[29] A. A. Hussein and I. Batarseh, "An overview of generic battery models," in *Proc. IEEE Power Energy Soc. General Meeting*, Detroit, MI, USA, 2011, pp. 1–6.
[30] W. Huang and J. A. Abu Qahouq, "An online battery impedance measurement method using DC–DC power converter control," *IEEE Trans. Ind. Electron.*, vol. 61, no. 11, pp. 5987–5995, Nov. 2014.
[31] M. Einhorn, F. V. Conte, C. Kral, and J. Fleig, "A method for online capacity estimation of lithium ion battery cells using the state of charge and the transferred charge," in *Proc. IEEE Int. Conf. Sustain. Energy Technol.*, 2010, pp. 1–6.
[32] S. Abu-Sharkh and D. Doerffel, "Rapid test and non-linear model characterisation of solid-state lithium-ion batteries," *J. Power Sources*, vol. 130, nos. 1/2, pp. 266–274, May 2004.
[33] J. Li *et al.*, "Bandwidth based electrical-analogue battery modeling for battery modules," *J. Power Sources*, vol. 218, pp. 331–340, Nov. 2012.
[34] M. Petzl and M. A. Danzer, "Advancements in OCV measurement and analysis for lithium-ion batteries," *IEEE Trans. Energy Convers.*, vol. 28, no. 3, pp. 675–681, Sep. 2013.
[35] C. Weng, J. Sun, and H. Peng, "A unified open-circuit-voltage model of lithiumion batteries for state-of-charge estimation and state-of-health monitoring," *J. Power Sources*, vol. 258, pp. 228–237, Jul. 2014.
[36] B. Pattipati *et al.*, " Open circuit voltage characterization of lithium-ion batteries, "*J. Power Sources*, vol. 269, pp. 317–333, Dec. 2014.
[37] Y. Xing *et al.*, "State of charge estimation of lithiumion batteries using the open-circuit voltage at various ambient temperatures," *Appl. Energy*, vol. 113, pp. 106–115, Jan. 2014.
[38] M. Dubarry, N. Vuillaume, and B. Y. Liaw, "From single cell model to battery pack simulation or Li-ion," *J. Power Sources*, vol. 186, no. 2, pp. 500–507, Jan. 2009.
[39] L. Maharjan, S. Inoue, and H. Akagi, "A transformerless energy storage system based on a cascade multilevel PWM converter with star configuration," *IEEE Trans. Ind. Appl.*, vol. 44, no. 5, pp. 1621–1630, Sep./Oct. 2008.
[40] C. Cecati, A. Dell'Aquila, M. Liserre, and V. G. Monopoli, "Design of H-bridge multilevel active rectifier for traction systems," *IEEE Trans. Ind. Appl.*, vol. 39, no. 5, pp. 1541–1550, Sep./Oct. 2003.
[41] C. Cecati, A. Dell'Aquila, M. Liserre, and V. G. Monopoli, "A passivity-based multilevel active rectifier with adaptive compensation for traction applications," *IEEE Trans. Ind. Appl.*, vol. 39, no. 5, pp. 1404–1413, Sep./Oct. 2003.
[42] A. Dell'Aquila, M. Liserre, V. G. Monopoli, and P. Rotondo, "An energy-based control for an n-H-bridges multilevel active rectifier," *IEEE Trans. Ind. Electron.*, vol. 52, no. 3, pp. 670–678, Jun. 2005.
[43] A. Dell'Aquila, M. Liserre, V. G. Monopoli, and P. Rotondo, "Overview of PI-based solutions for the control of DC buses of a single-phase H-bridge multilevel active rectifier," *IEEE Trans. Ind. Appl.*, vol. 44, no. 3, pp. 857–866, May/Jun. 2008.
[44] Y. Yu, G. Konstantinou, B. Hredzak, and V. G. Agelidis, "Power balance of cascaded H-bridge multilevel converters for large-scale photovoltaic integration," *IEEE Trans. Power Electron.*, vol. 31, no. 1, pp. 292–303, Jan. 2016.
[45] Y. Yu, G. Konstantinou, B. Hredzak, and V. G. Agelidis, "On extending the energy balancing limit of multilevel cascaded H-bridge converters for large-scale photovoltaic farms," in *Proc. Australas. Univ. Power Eng. Conf.*, 2013, pp. 1–6.
[46] P. Sochor and H. Akagi, "Theoretical comparison in energy-balancing capability between star- and delta-configured modular multilevel cascade inverters for utility-scale photovoltaic systems," *IEEE Trans. Power Electron.*, vol. 31, no. 3, pp. 1980–1992, Mar. 2016.

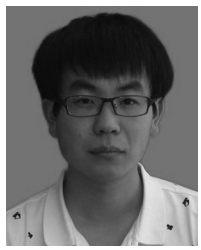

Chang Liu was born in Xuzhou, Jiangsu, China, in 1992. He received the B.Eng. degree in electrical engineering from the China University of Mining and Technology, Jiangsu, China, in 2017. He is currently working toward the Ph.D. degree with Wind Power Research Center, School of Electronic Information and Electrical Engineering, Shanghai Jiao Tong University, Shanghai, China.

His current research interests include large power battery storage systems, power conversion systems, and multilevel converters.

Ning Gao was born in Haining, Zhejiang, China, in 1987. He received the B.S. degree in electronics and information engineering from Zhejiang University, Hangzhou, China, in 2009, and the M.S. and Ph.D. degrees from Shanghai Jiao Tong University, Shanghai, China, in 2011 and 2017, respectively.

Since June 2017, he has been with the Department of Electrical Engineering, Shanghai Maritime University, Shanghai, China, where he is currently working as a Lecturer. His current research interests include power converters applied in battery energy storage systems.

Xu Cai received the B.Eng. degree from Southeast University, Nanjing, China, in 1983, and the M.Sc. and Ph.D. degrees from the China University of Mining and Technology, Jiangsu, China, in 1988 and 2000, respectively.

From 1989 to 2001, he was an Associate Professor with the Department of Electrical Engineering, China University of Mining and Technology. In 2002, he joined Shanghai Jiao Tong University, as a Professor, and is the Director of Wind Power Research Center, Shanghai Jiao Tong University since 2008. He was the first Executive Deputy Director of State Energy Smart Grid R&D Center, Shanghai, from 2010 to 2013. His special fields of interest include power electronics and renewable energy exploitation and utilization, including wind power converters, wind turbine control systems, large power battery storage systems, and wind farms and grid integration with HVdc.

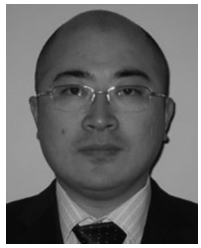

Rui Li (S'10–M'11) was born in Qingdao, China, in 1980. He received the M.S. degree in electrical engineering from the Nanjing University of Aeronautics and Astronautics, Nanjing, China, in 2005, and the Ph.D. degree in electrical engineering from Zhejiang University, Hangzhou, China, in 2010.

From September 2008 to August 2009, he was an Academic Guest with Power Electronic Systems Laboratory, Swiss Federal Institute of Technology, Zurich, Switzerland. From July 2014 to August 2015, he was a Postdoctoral Research Scholar with the Center for Advanced Power Systems, Department of Electrical and Computer Engineering, College of Engineering, Florida State University, Tallahassee, FL, USA. Since 2010, he has been with the Department of Electrical Engineering, School of Electronics, Information and Electrical Engineering, Shanghai Jiao Tong University, Shanghai, China, where he is currently an Associate Professor. His current research interests include applications of power electronics in renewable energy conversion.

Dr. Li was the recipient of the IEEE Power Electronics Society Transactions Second Prize Paper Award in 2015.